IEEE Access
Multidisciplinary ⋮ Rapid Review ⋮ Open Access Journal

Received 29 November 2023, accepted 17 December 2023, date of publication 19 December 2023,
date of current version 28 December 2023.

Digital Object Identifier 10.1109/ACCESS.2023.3344768

RESEARCH ARTICLE

A High-Gain Filtering Fabry-Perot Antenna With RCS Reduction

TRUONG LE-HUU[1], HAI DANG LE[1], (Member, IEEE), SON XUAT TA[1], (Senior Member, IEEE), KHAC KIEM NGUYEN[1], (Member, IEEE), AND NGHIA NGUYEN-TRONG[2], (Senior Member, IEEE)

[1]School of Electrical and Electronic Engineering, Hanoi University of Science and Technology, Hanoi 100000, Vietnam
[2]School of Electrical and Electronic Engineering, The University of Adelaide, Adelaide, SA 5005, Australia

Corresponding author: Son Xuat Ta (xuat.tason@hust.edu.vn)

This work was supported by the Vietnam National Foundation for Science and Technology Development (NAFOSTED) under Grant 102.04-2021.06.

ABSTRACT A high-gain filtering Fabry-Perot antenna (FPA) with radar cross section (RCS) reduction is proposed. The design utilizes a partially reflecting surface (PRS) which is integrated with a chessboard arranged metasurface (CAMS) in a single-layered substrate. The CAMS is composed of periodic strip arrays to reduce monostatic RCS based on the phase cancellation principle. The PRS structure is a cross-slot array which is designed to work with both orthogonal orientations of the CAMS elements while yielding a high reflection magnitude. Accordingly, the proposed FPA achieves a high-gain broadside radiation and wideband RCS reduction. The filtering functionality is achieved from a T-shaped feed patch, which is, interestingly, enhanced by the integration of CAMS in the PRS. For validation, a prototype operating at 6.0 GHz has been fabricated and measured. The antenna with an overall size of $3.2\lambda_0 \times 3.2\lambda_0 \times 0.57\lambda_0$ at 6.0 GHz exhibits an impedance matching bandwidth (BW) of 5.73−6.23 GHz, a 3-dB gain BW of 5.76−6.17 GHz with the peak gain of 14.63 dBi, and an out-of-band suppression of $\geq$ 20 dB. Meanwhile, it achieves an RCS-reduction bandwidth of about 4.0 to 9.0 GHz (76.9%).

INDEX TERMS Fabry-Perot antennas (FPA), partially reflecting surface, radar cross section, chessboard arrangement, polarization conversion, filtering antenna.

I. INTRODUCTION

Fabry-Perot antennas (FPAs) [1], also named as resonant cavity antennas, basically consist of a simple source in a parallel-plate cavity constructed with a ground plane (GND) at the bottom and a partially reflecting surface (PRS) at the top. Owing to the features of high gain with simple structure, the FPAs are attractive in various applications such as onboard satellites, air-craft, and unmanned aerial vehicles. For safety in these applications, stealth characteristic or low radar cross section (RCS) is critically required. Generally, the antenna, which contains several metallic components, has a considerable contribution to the overall RCS of the platform. Accordingly, FPAs with RCS reduction have been received substantial attention in the last decade. Different methods have been presented for reducing the RCS of FPAs, which are summarized as follows:

1) An effective method for wideband operation is adding absorbing structure to the PRS, which was first presented in [2]. For easy implementation, the absorber-integrated PRS is built on a single-layered substrate [2], [3], [4], [5], [6], i.e., the PRS is patterned on the bottom side to ensure a high reflectivity for the enhanced gain of FPA, whereas the absorber structure is placed on the top side to absorb incoming waves. Typically, metallic square loops with mounted resistors are employed, however, they may degrade the antenna efficiency. Recently, multi-layered PRSs have been presented to improve the performances of RCS-reduction FPAs such as enhancing band-pass response [7], radiation pattern [8], and reducing RCS for both co- and cross-polarized incident

The associate editor coordinating the review of this manuscript and approving it for publication was Davide Comite.

waves [9]. The multi-layered configurations, however, increase the complexity and realization cost of the antenna.

2) Another common approach is based on the phase cancellation principle of chessboard arranged metasurface (CAMS) [10] which is a combination of artificial magnetic conductor (AMC) and perfect electric conductor (PEC) cells. Since the AMC and PEC cells have opposite reflection phases, for any normal incident wave, the reflections from CAMS cancel out, and consequently, the monostatic RCS is reduced. Following this approach, many polarization conversion surfaces (PCS), which yield $180 \pm 30°$ reflection phase variations between two neighboring cells, have been used in FPAs to reduce RCS within a wide frequency range [11], [12], [13], [14], [15], [16], [17], [18], [19].
3) Several other techniques were also applied in FPAs for RCS reduction, which include coding metasurface [20], [21], phase gradient metasurface [22], [23], receiver-transmitter metasurface [24], phase delay line [25], asymmetric electromagnetic absorption [26]. These techniques are effective only in a typically narrow bandwidth.

Besides the desired operational bandwidth, the aforementioned FPAs commonly yield undesired radiations, e.g., high-order resonant modes, which could degrade the stealth characteristic. To suppress the undesired radiations, filtering antennas, which are designed for achieving both antenna and filter function in a single structure, have been considered as an efficient solution [27]. Also, the filtering antennas contribute to reduce losses, complexity, size, and cost in microwave devices. For higher gain, the filtering antennas are traditionally arrayed in the previous works, such as [28], [29], [30], and [31], which require complicated feeding networks and design configurations. Recently, a FPA with simple structure has been reported for both filtering and high-gain features [32]. However, this filtering FPA did not yield the scattering reduction.

This paper presents an FPA concept that can improve the filtering characteristics while still providing RCS reduction and keeping a simple configuration, i.e., with a single-layered substrate. The design employs a PRS integrated with a CAMS. The PRS unit cell is carefully designed to work in two orthogonal orientations of the CAMS elements, thus enabling the use of chessboard arrangement to reduce RCS while keeping the PRS functionality. Interestingly, the CAMS-integrated PRS also exhibits filtering characteristics, which is used together with the feeding patch to obtain the overall filtering performance of the design.

II. ANTENNA DESIGN AND CHARACTERISTICS

A. CAMS-INTEGRATED FPA DESIGN

Fig. 1 shows the schematic model of the proposed FPA which includes a feed source in a parallel-plate cavity formed by a conducting GND and a CAMS-integrated PRS.

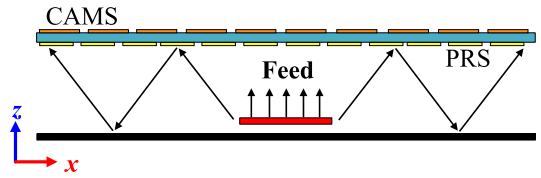

FIGURE 1. Schematic model of the proposed FPA.

For completion, we briefly summarize the classical theory of FPA in [33] in the following. For a FPA, a radiation at the broadside is obtained when the reflection phase of the PRS (Φ_{PRS}) is theoretically the same as

$$\Phi_1(f) = \frac{4\pi f}{c} H_c + (2N-1)\pi, \quad N = 0, 1, 2, \ldots \tag{1}$$

where f is the frequency, c is the speed of light in free space, H_c is the cavity height and is chosen a value of approximately $\lambda_0/2$ (λ_0 is the wavelength in free-space at the resonance frequency). When (1) is satisfied and the PRS size is sufficiently large, the total directivity of the FPA (D_{total} in dB scale) can be given by [34]

$$D_{total} = D_{source} + D_{PRS} \tag{2}$$

where D_{source} is directivity of the feed source, D_{PRS} is the enhanced-directivity due to the PRS. D_{PRS} is depended on the reflection magnitude of the PRS, $|\Gamma_{PRS}|$, as follows

$$D_{PRS} = 10\log_{10}\frac{1+|\Gamma_{PRS}|}{1-|\Gamma_{PRS}|} \tag{3}$$

Equation (3) indicates that the PRS needs to yield a large value of $|\Gamma_{PRS}|$, i.e., close to 1 (or 0 dB), to obtain a high value of D_{total}.

The CAMS is designed utilizing the top conductive layer of the PRS (Fig. 1). It is implemented based on the phase cancellation principle [10] to reduce RCS within a wide frequency range. To utilize this principle, two units of CAMS are arranged in a chessboard configuration. These two units need to reflect the x- and y-polarized incident waves with a reflection phase difference of ideally 180°. A typical satisfactory range for this phase difference is $180° \pm 30°$ [11], [12], [13], [14], [15], [16], [17].

B. UNIT CELL DESIGN

The proposed unit cell is illustrated in Fig. 2(a). It consists of two layers of metallic patterns placed on both sides of a single-layered substrate (F4BM sheet, $\varepsilon_r = 2.65$, $\tan\delta = 0.002$). The bottom side is a metallic coat with a symmetrical cross slot, while the top side is a metallic strip. Fig. 2(b) shows its simulation model in the ANSYS Electronics Desktop. The unit cell is characterized using periodic boundary conditions along the x- and y-directions, and two Floquet ports along $\pm z$ directions. This CAMS-integrated PRS is designed to operate around 6.0 GHz and its optimized parameters are given in the caption of Fig. 2.

In order to realize both PRS and CAMS functionality, the following conditions need to satisfy

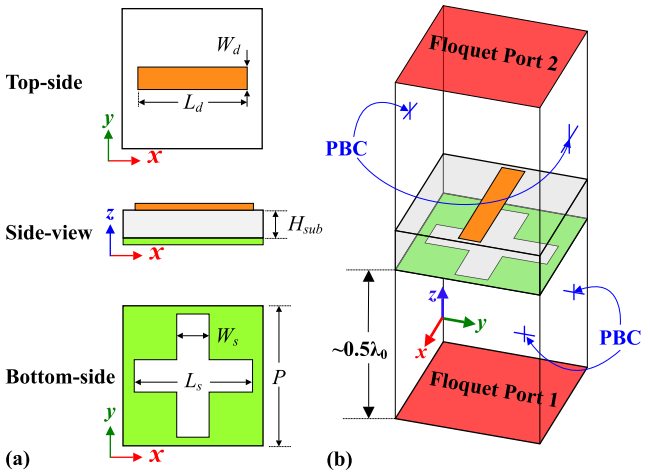

FIGURE 2. (a) Structure of PRS integrated CAMS: $P = 13$, $W_d = 2$, $L_d = 12$, $H_{sub} = 4$, $W_s = 3.6$, $L_s = 12$ (unit: mm); (b) simulation model for the unit-cell.

1) For both x-polarized and y-polarized wave, the reflection magnitude of PRS, i.e., $|\Gamma_{PRS}|$ (or $|S_{11}^x|$ and $|S_{11}^y|$) has to be sufficiently high, according to (3).
2) The reflection phases of the CAMs for the incident x-polarized and y-polarized incoming waves exhibit about 180° phase difference, i.e., $\angle S_{22}^x - \angle S_{22}^y \approx 180°$, according to the phase cancellation principle using CAMS [10].

Fig. 3 shows the three steps to realize the proposed unit cell structure and their corresponding scattering properties. The initial design (Step 1) consists of a metallic strip printed on a grounded substrate. A slot is etched on the bottom side of the initial design to create Step 2. Finally, a cross slot is used at the bottom side to establish the proposed structure. For demonstration, the parameters in all steps are the same as those of the final design (given in the caption of Fig. 2).

As shown in Fig. 3(b), at 6 GHz, Step-1 design acts as an AMC for the x-polarized incident wave ($\angle S_{22}^x \approx 0°$), but as a nearly PEC for the y-polarized incident wave ($\angle S_{22}^y \approx 150°$). This results show the potential of using metallic strips in a chessboard arrangement to reduce RCS. Nevertheless, the design in Step 1 totally blocks the incident wave from the feed since the bottom side of substrate is fully metal, i.e., $|S_{22}^{x,y}| = 1$, and $|S_{11}^{x,y}| = 1$.

To allow the structure to work as a PRS, a slot along x-direction at etched on the GND in Step-2. This configuration allows the y-polarized waves passing through itself, but reflects the x-polarized waves. Accordingly, the reflection property for the y-polarization is impacted significantly, whereas it hardly changes for the x-polarization (see the all red curves in Fig. 3(b)-(f)). It is noted that the Step-2 design yields a reflection phase difference of about 90° between the two polarizations, which should be re-adjusted if one wants the design to work as a CAMS for RCS reduction.

Thanks to the cross slot in the GND, the proposed design (Step 3) achieves all desired scattering properties (see the all blue curves in Fig. 3(b)-(f)): For the illumination from Floquet port 2, the reflection phase difference is 180° ± 30° from 5 to 7 GHz. For the illumination from the Floquet port 1, the structure yields a resonant frequency of $f_r = 6$ GHz for the broadside radiation of FPA and a high reflectivity ($|S_{11}^{x,y}| \geq 0.8$) at around 5.8 to 6 GHz. Following equation (3), the proposed PRS can theoretically provide an enhanced directivity of about 9.5 dB for the FPA.

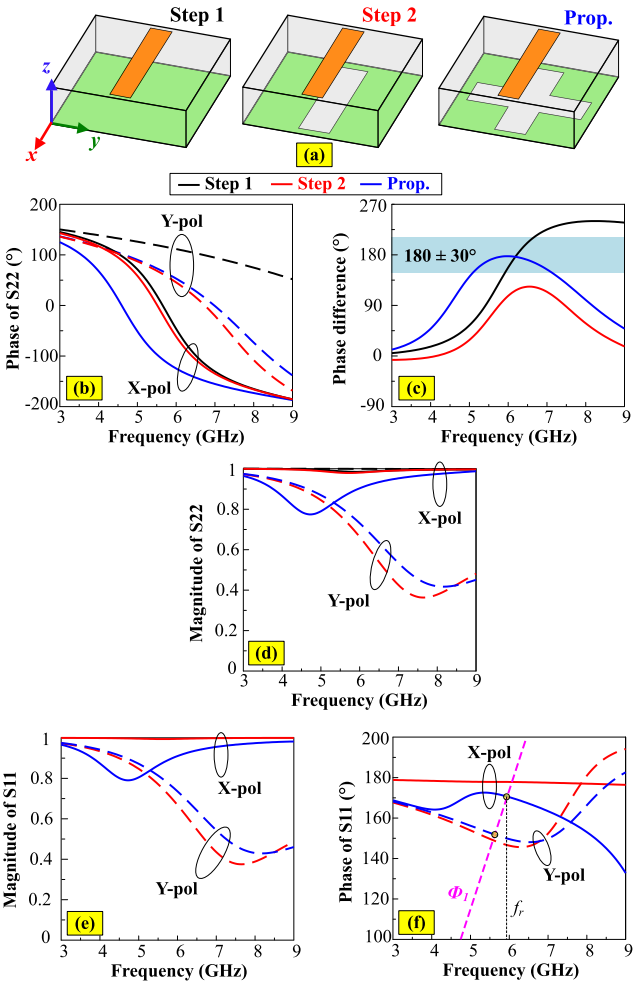

FIGURE 3. (a) Three steps to establish the unit-cell of PRS integrated CAMS and (b-f) their simulated scattering properties.

One interesting feature of this design concept is that it can enhance the filtering (frequency selectivity) characteristics of the FPA. The results in Fig. 3(e) indicate that the FPA only works with high gain enhancement in the vicinity of $5.5 - 6$ GHz. Out of this range, especially at high frequency, the magnitude of $|S_{11}^y|$ is low, which significantly reduces the antenna gain at high frequency. This effect will be demonstrated in the later section.

C. ANTENNA GEOMETRY

After the scattering properties of the PRS unit-cell are fully characterized, the CAMS is formed and applied to

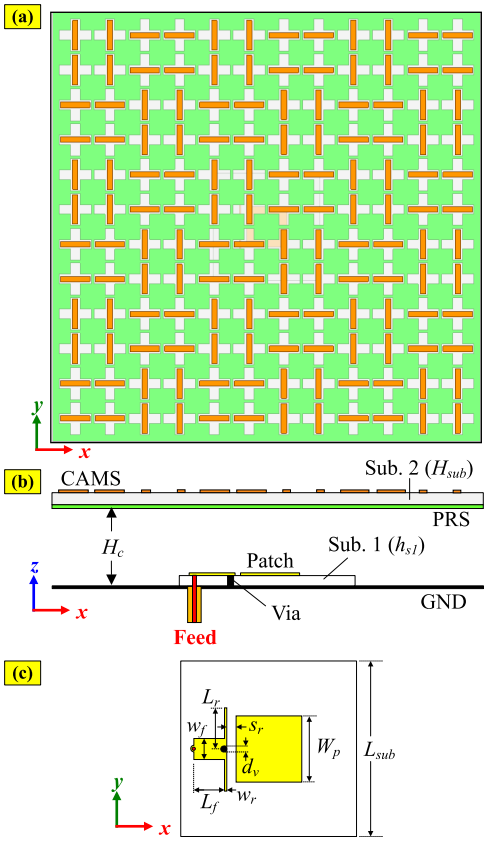

FIGURE 4. Geometry of the CAMS-integrated FPA: (a) top view, (b) side view, and (c) the source element of T-shaped feed patch. ($H_c = 24.5$, $H_{sub} = 4$, $h_{s1} = 1.5748$, $W_p = 15$, $d_v = 1.5$, $L_r = 9.5$, $S_r = 2$, $W_f = 4.85$, $L_f = 7$; unit: mm.)

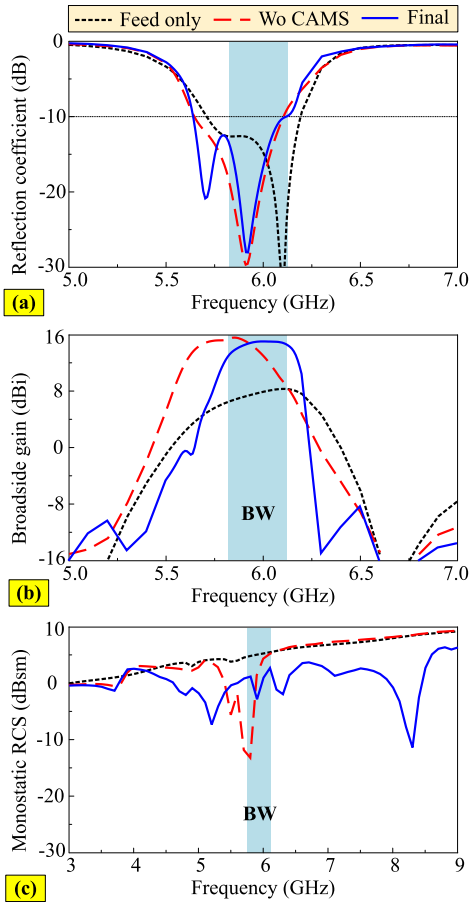

FIGURE 5. Performance comparison of the different antennas: (a) reflection coefficient, (b) broadside gain, and (c) monostatic RCS with Y-polarized incident wave.

establish the FPA (see Fig. 4). The PRS is suspended above a conducting GND to form a Fabry-Perot resonator cavity with height of H_c. A T-shaped feed patch adapted from [35] is employed as the source element of the FPA, as shown in Fig. 4(c). The source element is built on a 40×40-mm^2 Roger Duroid RT5880 substrate ($\varepsilon_r = 2.2$, $\tan\delta = 0.0009$, and thickness of h_{s1}) and mounted at the center of GND. The T-shaped feed consists of a microstrip-line, a pair of $\lambda/4$ resonators, and a shorting via, which provides a broad bandwidth and harmonic suppression. The antenna parameters optimized via ANSYS HFSS 2022 are given in the caption of Fig. 4. The final design has an overall size of $160 \times 160 \times 28.5$ mm^3.

D. ANTENNA PERFORMANCES

To illustrate the roles of the CAMS-integrated PRS, the antenna in different configurations, including the feed only, FPA without CAMS, and the proposed FPA design shown in Fig. 4, are investigated and compared in Fig. 5.

Thank to the T-shaped feed, the source element achieves a -10-dB impedance bandwidth (BW) of 5.7 - 6.2 GHz with two resonances at 5.75 and 6.10 GHz [Fig. 5(a)]. Also, the source yields a moderate filtering characteristic and an averaged gain of about 6.0 dB within its impedance matching BW [see Fig. 5(b)]. With the large conducting GND, the source yields a monostatic RCS value similar to the same-size copper plate [Fig. 5(c)].

By adding the PRS without CAMS, the resonances slightly shifted toward the lower frequency, whereas the broadside gain is enhanced significantly. The FPA configuration without CAMS achieves a BW of $5.6 - 6.1$ GHz for -10-dB reflection coefficient [Fig. 5(a)] and a 3-dB gain BW of $5.55 - 6.0$ GHz with the peak value of 15.7 dBi [Fig. 5(b)]. From Fig. 5(c), the antenna without CAMS yields a RCS reduction within a small frequency range of $5.2 - 6.0$ GHz.

With the CAMS-integrated PRS, the antenna achieves a broadband RCS reduction. At the same time, the filtering characteristic is significantly enhanced with a much higher roll-off rate at the upper frequency range. These results agree well with the theoretical prediction about filtering performance mentioned in Section II-B, and demonstate the effectiveness of the proposed design approach. This is the main contribution of the paper. Finally, Fig. 5(c) indicates an avarage of about 5-dB RCS reduction in a wide bandwidth from 4.5 GHz to 8.5 GHz.

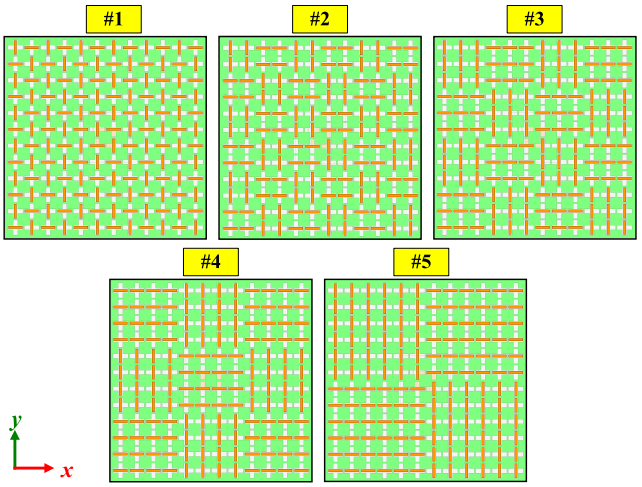

FIGURE 6. Different CAMS configurations of the proposed FPA.

E. CAMS ARRANGEMENTS

With the aim of achieving a better wideband RCS reduction, in this sub-section, we will investigate how the performance varies with different CAMS arrangements, as shown in Fig. 6. The results are illustrated in Fig. 7. Since the PRS integrated CAMS is designed to realize both PRS and CAMS functionality simultaneously, the size of effective CAMS cell strongly impacts the RCS reduction, but hardly impacts the radiation performance of the proposed antenna. As shown in Figs. 7(a, b), the reflection coefficient and broadside gain slightly change for different CAMS arrangements. From Fig. 7(c), the effective cell of CAMS needs at least two adjacent cells contributing together to obtain the wideband RCS reduction. Moreover, there is a trade-off between the gain roll-off rate and the RCS reduction performance. Filtering performance is the best with #2 configuration while the RCS reduction performance is maximized with a wider bandwidth for #4 configuration. As our primary aim is to achieve an optimal performance in RCS reduction while filtering performance is partly provided by the feeding structure, we select #4 design for fabrication and validation. Nevertheless, it should be indicated that #2 should be used if a high roll-off rate in realized gain is required.

F. ARBITRARY POLARIZATION INCIDENCES

To further confirm the feature of RCS reduction, the proposed FPA (with configuration #4 in Fig. 6) is illuminated by arbitrary polarization incidences, including X- ($\phi = 0°$), Y- ($\phi = 90°$), and D- ($\phi = 45°$) polarizations and its monostatic RCS values are given in Fig. 8. As compared to a reference metallic plate with the same aperture of 160 × 160 mm^2, the proposed FPA using CAMS-integrated PRS achieves a wideband RCS reduction with different polarizations of the incident waves. Although the RCS-reduction bandwidths for the $X-$ and $D-$polarized illuminations are slightly narrower than the Y-polarization, they are still relatively large, i.e, from 4.5 to 9.0 GHz. Also, for all polarizations, the RCS reduction is slightly degraded at the

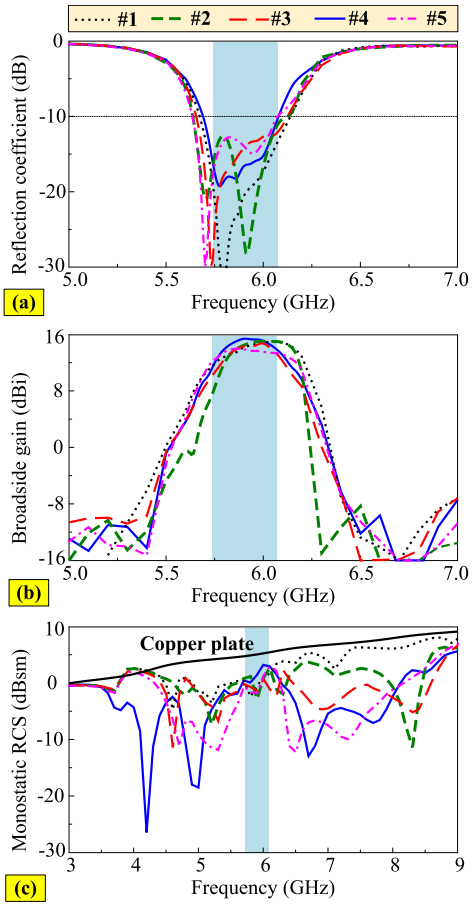

FIGURE 7. Performances of the proposed FPA for different CAMS arrangements: (a) reflection coefficient, (b) broadside gain, and (c) monostatic RCS with Y-polarized illumination.

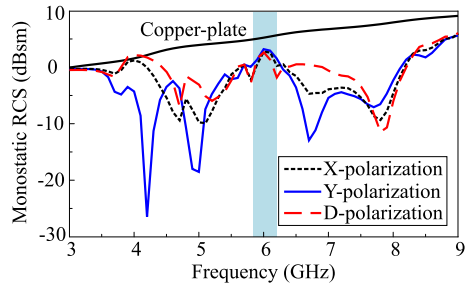

FIGURE 8. Simulated monostatic RCS under normal incidences with arbitrary polarization.

in-band. This has been a common problem in most of the RCS-reduction antennas using CMAS structures, e.g., [11], [12], [13], [14], [15], [16], [17], [18], and [19]. Nevertheless, the proposed design achieves the minimum RCS reduction of about 3 dB at 6 GHz, as shown in Fig. 8.

III. FABRICATION AND MEASUREMENT

A. FABRICATED PROTOTYPE

As mentioned above, the proposed FPA with configuration #4 of CAMS (in Fig. 6) is fabricated and measured. Fig. 9 shows a fabricated prototype with an overall size of 160 × 160 × 28.5 mm^3 ($3.2\lambda_0 \times 3.2\lambda_0 \times 0.57\lambda_0$ at 6 GHz).

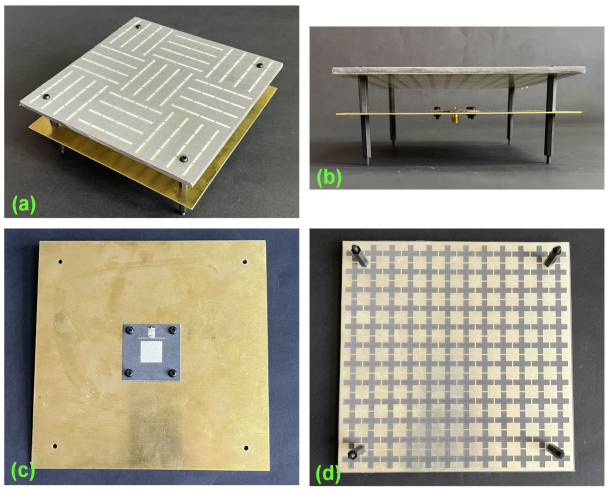

FIGURE 9. Fabricated prototype of the proposed antenna: (a) perspective view, (b) side view, (c) the source element of T-shaped feed patch, and (d) back side of PRS integrated CAMS.

The components, including the source and PRS-integrated CAMS, are fabricated via a standard printed circuit board (PCB) technology, meanwhile a copper plate with 1-mm thickness is used as the GND. Plastic hexagonal posts and screws ($\varepsilon_r = 2.0$, $\tan\delta = 0.02$, and diameter of 6 mm) are employed to construct the antenna prototype.

B. RADIATION PERFORMANCES

Fig. 10(a) shows the simulated and measured reflection coefficients of the antenna prototype. There is a good agreement between the simulation and measurement and both indicate that the antenna has very low realized gain in the out-of-band region (i.e., there is not any higher-order radiating mode in the high frequency region up to 15 GHz). The measurement results in a −10-dB impedance bandwidth

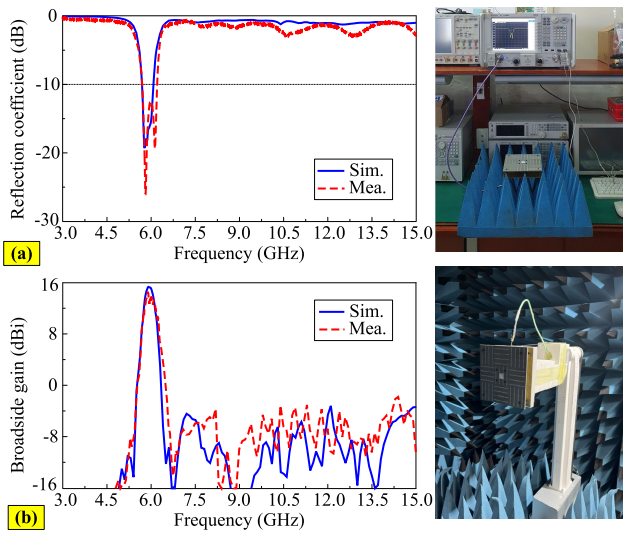

FIGURE 10. (a) S-parameters and (b) realized broadside gain of the prototype.

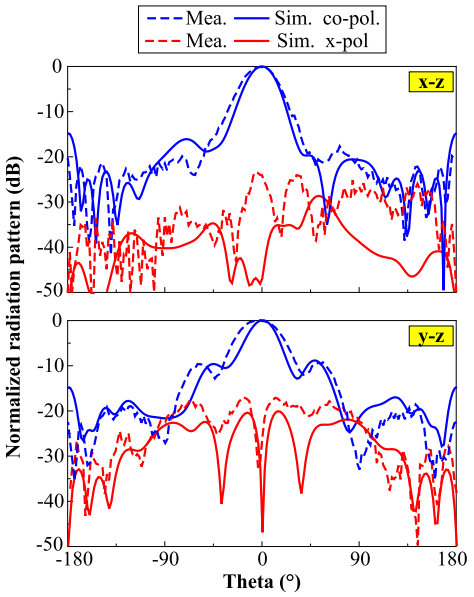

FIGURE 11. Normalized radiation pattern of the FPA prototype at 6.0 GHz.

of 5.73 − 6.23 GHz, whereas the simulated bandwidth is 5.70 − 6.07 GHz. A slight discrepancy between the simulation and measurement could be attributed to the different permittivities of the substrates in full-wave simulator and realization.

The realized broadside gain of the FPA prototype is given in Fig. 10(b). The measurements result in the peak gain of 14.6 dBi and a 3-dB gain bandwidth of 5.76 − 6.17 GHz, while the simulations result in the corresponding values of 15.4 dBi and 5.76 − 6.12 GHz, respectively. Moreover, the antenna yields a very good filtering characteristic; i.e., both simulation and measurement yield an out-of-band suppression of $\geq$ 24 dB in the low-frequency region (3 − 5.5 GHz) and $\geq$ 20 dB in the high frequency region (6.5 − 15.0 GHz).

Fig. 11 illustrates the 6-GHz normalized radiation patterns of the fabricated prototype. It is observed that the proposed FPA achieves an excellent broadside radiation with quite symmetrical pattern, low cross-polarization level, and high front-to-back ratio. At 6.0 GHz, the measurements result in a cross-polarization level of ≤ -20 dB, front-to-back ratio of $\geq$ 15 dB, and half-power beamwidths of 26° and 24° in the *xz* and *yz*-planes, respectively.

C. SCATTERING PERFORMANCES

The RCS of the proposed FPA is measured in a laboratory environment. We used two single-ended wideband dual-polarized Vivaldi antennas in [36] as transmitter (Tx) and receiver (Rx) which were connected to two ports of a Keysight N5244A PNA-X microwave network analyzer. The proposed FPA was illuminated at a distance of 1 m away from the Tx antenna. For normal incidence, the separation angle between Tx and Rx was set 10° because of the finite size of the prototype. Fig. 12 shows the simulated and measured

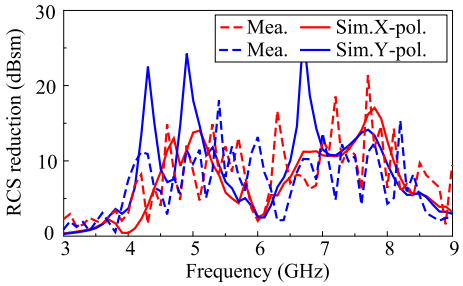

FIGURE 12. Simulation and measurement RCS reduction of the FPA prototype.

TABLE 1. A comparison of the proposed FPAs with the related works.

Ant.	Overall size (λ_c)	Structure	Radiation BW (GHz)	Peak gain (dBi)	RCSR BW (GHz)	Filtering
[11]	1.25×1.25 × 0.58	FPA	9.2-10.1 (8.8%)	10.6	9-20 (75.9%)	NO
[12]	1.80×1.80 × 0.45	FPA1	8.25-9.5 (13.8%)	11.2	6-14 (80%)	NO
[13]	2.30×2.30 × 0.69	FPA	9.4-11.4 (18.6%)	12.0	8.0-18 (76.9%)	NO
[14]	4.90×4.90 × 0.71	FPA	26.7-34.2 (24.6%)	20.0	28-48 (52%)	NO
[15]	2.6×2.6 × 0.45	FPA	9.5-12.8 (11.6%)	13.4	6-15 (85.7%)	NO
[16]	2.7×2.7 × 0.71	FPA	8.9-11.5 (25.5%)	17.2	8-26 (105.9%)	NO
[17]	2.8×2.8 × 0.71	FPA	8.6-11.1 (25.4%)	17.1	8.6-14 (47.8%)	NO
[28]	2.8×4.6 × 1.43	4×4 array	9.5-10.5 (10.5%)	20.4	N/A	YES
[29]	2.0×1.4 × 0.09	2×2 array	2.5-3.6 (37.1%)	12.4	N/A	YES
[30]	4.1×4.1 × 1.26	4×4 array	27.3-30.8 (12.05%)	20.6	N/A	YES
[31]	1.52×1.52 × 0,02	2×2 array	3.4-3.6 (4.26%)	12.2	N/A	YES
[32]	2.2×2.2 × 0.51	FPA	5.02-5.96 (17.1%)	13.0	N/A	YES
Prop.	3.2×3.2 × 0.57	FPA	5.73-6.23 (8.36%)	14.6	4.0-9.0 (76.9%)	YES

BW: bandwidth; RCSR: RCS reduction; λ_c is the free space wavelength referring to the center frequency of the radiation bandwidth; N/A: not available

RCS reduction of the FPA prototype for the x- and y-polarized illuminations. The RCS reduction values are obtained by comparing the scattering fields of the FPA prototype and a reference metallic plate with the same aperture of 160 × 160 mm^2. Both simulation and measurement indicate that the proposed antenna achieves an RCS reduction within a wide frequency range. The measurements result in the peak RCS reduction of 20 dB, whereas the simulations result in the corresponding values of 28.4 dB.

D. COMPARISON AND DISCUSSION

Table 1 shows a comparison of the proposed design and the related works, including non-FPA antennas with high gain and filtering performances [11], [12], [13], [14], [15], [16], [17], [28], [29], [30], [31], [32]. It should be noted that this study targets a design with filtering performance, which is often required for narrow band operation so the radiation bandwidth is not a figure of merit in this particular case of comparison.

For the radiation characteristic, as compared to the priors [11], [12], [13], [14], [15], [16], [17], the proposed FPA yields comparable performances in terms of aperture size and broadside gain. Thanks to the utilization of CAMS, all configurations achieve a wideband RCS reduction. Nevertheless, it should be emphasized that compared to all other FPAs, our design introduces the filtering characteristics using a very simple CAMS-integrated PRS (one substrate layer with only one type of PRS unit-cell), which is unique among others. As compared to the existing designs with high-gain and filtering features [28], [29], [30], [31], [32], only our FPA achieves RCS reduction.

IV. CONCLUSION

A high-gain FPA with wideband RCS reduction has been demonstrated. It employs a single-layered PRS-integrated CAMS which is deliberately designed to achieve three functions simultaneously: (i) ensuring a high reflectivity for the high-gain of FPA; (ii) reducing RCS across a wide frequency range; (iii) enhanced filtering performance. The final prototype with overall size of $3.2\lambda_0 \times 3.2\lambda_0 \times 0.57\lambda_0$ at 6.0 GHz yields a −10-dB reflection coefficient BW of 5.73−6.23 GHz and a 3-dB gain BW of 5.76−6.17 GHz with the peak gain of 14.6 dBi. Meanwhile, the prototype achieves an average of roughly 5-dB RCS reduction across a wide bandwidth from 4.0 to 9.0 GHz. A very good filtering performance has been realized with more than 24 dB and 20 dB suppression level in the lower and upper frequency range, respectively. Thanks to these advantages, the proposed design can be a good candidate for used in radar systems, satellites, aircraft, as well as unmanned aerial vehicles.

REFERENCES

[1] R. M. Hashmi and K. P. Esselle, *Resonant Cavity Antennas*. Hoboken, NJ, USA: Wiley, 2019, pp. 1–20. [Online]. Available: https://onlinelibrary.wiley.com/doi/abs/10.1002/047134608X.W8385

[2] W. Pan, C. Huang, P. Chen, X. Ma, C. Hu, and X. Luo, "A low-RCS and high-gain partially reflecting surface antenna," *IEEE Trans. Antennas Propag.*, vol. 62, no. 2, pp. 945–949, Feb. 2014.

[3] H. Jiang, Z. Xue, W. Li, W. Ren, and M. Cao, "Low-RCS high-gain partially reflecting surface antenna with metamaterial ground plane," *IEEE Trans. Antennas Propag.*, vol. 64, no. 9, pp. 4127–4132, Sep. 2016.

[4] C. Huang, W. Pan, X. Ma, and X. Luo, "A frequency reconfigurable directive antenna with wideband low-RCS property," *IEEE Trans. Antennas Propag.*, vol. 64, no. 3, pp. 1173–1178, Mar. 2016.

[5] J. Mu, H. Wang, H. Wang, and Y. Huang, "Low-RCS and gain enhancement design of a novel partially reflecting and absorbing surface antenna," *IEEE Antennas Wireless Propag. Lett.*, vol. 16, pp. 1903–1906, 2017.

[6] J. Ren, W. Jiang, K. Zhang, and S. Gong, "A high-gain circularly polarized Fabry–Pérot antenna with wideband low-RCS property," *IEEE Antennas Wireless Propag. Lett.*, vol. 17, no. 5, pp. 853–856, May 2018.

[7] W. Yu, Y. Yu, W. Wang, X. H. Zhang, and G. Q. Luo, "Low-RCS and gain-enhanced antenna using absorptive/transmissive frequency selective structure," *IEEE Trans. Antennas Propag.*, vol. 69, no. 11, pp. 7912–7917, Nov. 2021.

[8] X. Liu, Z. Yan, E. Wang, T. Zhang, and F. Fan, "Magnetoelectric dipole-fed Fabry–Pérot antenna with wideband RCS reduction based on multilayer metasurface," *IEEE Antennas Wireless Propag. Lett.*, vol. 20, no. 7, pp. 1342–1346, Jul. 2021.

[9] J. Zhang, Y. Liu, Y. Jia, and R. Zhang, "High-gain Fabry–Pérot antenna with reconfigurable scattering patterns based on varactor diodes," *IEEE Trans. Antennas Propag.*, vol. 70, no. 2, pp. 922–930, Feb. 2022.

[10] M. Paquay, J.-C. Iriarte, I. Ederra, R. Gonzalo, and P. de Maagt, "Thin AMC structure for radar cross-section reduction," *IEEE Trans. Antennas Propag.*, vol. 55, no. 12, pp. 3630–3638, Dec. 2007.

[11] M. Long, W. Jiang, and S. Gong, "Wideband RCS reduction using polarization conversion metasurface and partially reflecting surface," *IEEE Antennas Wireless Propag. Lett.*, vol. 16, pp. 2534–2537, 2017.

[12] K. Li, Y. Liu, Y. Jia, and Y. J. Guo, "A circularly polarized high-gain antenna with low RCS over a wideband using chessboard polarization conversion metasurfaces," *IEEE Trans. Antennas Propag.*, vol. 65, no. 8, pp. 4288–4292, Aug. 2017.

[13] Y. Zheng, J. Gao, Y. Zhou, X. Cao, H. Yang, S. Li, and T. Li, "Wideband gain enhancement and RCS reduction of Fabry–Pérot resonator antenna with chessboard arranged metamaterial superstrate," *IEEE Trans. Antennas Propag.*, vol. 66, no. 2, pp. 590–599, Feb. 2018.

[14] S. Zarbakhsh, M. Akbari, F. Samadi, and A.-R. Sebak, "Broadband and high-gain circularly-polarized antenna with low RCS," *IEEE Trans. Antennas Propag.*, vol. 67, no. 1, pp. 16–23, Jan. 2019.

[15] Q. Chen and H. Zhang, "High-gain circularly polarized Fabry–Pérot patch array antenna with wideband low-radar-cross-section property," *IEEE Access*, vol. 7, pp. 8885–8889, 2019.

[16] Z. Liu, S. Liu, J. Bornemann, X. Zhao, X. Kong, Z. Huang, B. Bian, and D. Wang, "A low-RCS, high-GBP Fabry–Pérot antenna with embedded chessboard polarization conversion metasurface," *IEEE Access*, vol. 8, pp. 80183–80194, 2020.

[17] Z. Liu, S. Liu, X. Zhao, X. Kong, Z. Huang, and B. Bian, "Wideband gain enhancement and RCS reduction of Fabry–Pérot antenna using hybrid reflection method," *IEEE Trans. Antennas Propag.*, vol. 68, no. 9, pp. 6497–6505, Sep. 2020.

[18] H. Umair, T. B. A. Latef, Y. Yamada, T. Hassan, W. N. L. B. W. Mahadi, M. Othman, K. Kamardin, and M. I. Hussein, "Fabry–Pérot antenna employing artificial magnetic conductors and phase gradient metasurface for wideband monostatic RCS reduction and high gain tilted beam radiation," *IEEE Access*, vol. 9, pp. 66607–66625, 2021.

[19] Y.-F. Cheng, L. Yang, X. Zhong, C. Liao, and X. Ding, "Analysis and design of wideband low-RCS Fabry–Pérot antennas with reduced profile," *IEEE Trans. Antennas Propag.*, vol. 70, no. 9, pp. 7934–7943, Sep. 2022.

[20] L. Zhang, X. Wan, S. Liu, J. Y. Yin, Q. Zhang, H. T. Wu, and T. J. Cui, "Realization of low scattering for a high-gain Fabry–Pérot antenna using coding metasurface," *IEEE Trans. Antennas Propag.*, vol. 65, no. 7, pp. 3374–3383, Jul. 2017.

[21] L. Bai, X. G. Zhang, Q. Wang, C. X. Huang, W. X. Jiang, and T. J. Cui, "Dual-band reconfigurable metasurface-assisted Fabry–Pérot antenna with high-gain radiation and low scattering," *IET Microw., Antennas Propag.*, vol. 14, no. 15, pp. 1933–1942, Dec. 2020.

[22] Y. Jia, Y. Liu, W. Zhang, J. Wang, S. Gong, and G. Liao, "High-gain Fabry–Pérot antennas with wideband low monostatic RCS using phase gradient metasurface," *IEEE Access*, vol. 7, pp. 4816–4824, 2019.

[23] J. Yu, W. Jiang, and S. Gong, "Low-RCS beam-steering antenna based on reconfigurable phase gradient metasurface," *IEEE Antennas Wireless Propag. Lett.*, vol. 18, no. 10, pp. 2016–2020, Oct. 2019.

[24] P. Xie, G.-M. Wang, H.-P. Li, Y.-W. Wang, and B. Zong, "Wideband RCS reduction of high gain Fabry–Pérot antenna employing a receiver-transmitter metasurface," *Prog. Electromagn. Res.*, vol. 169, pp. 103–115, 2020.

[25] L. Gan, W. Jiang, Q. Chen, X. Li, and Z. Zhou, "Analysis and reduction on in-band RCS of Fabry–Pérot antennas," *IEEE Access*, vol. 8, pp. 146697–146706, 2020.

[26] T. D. Ha, L. Zhu, N. Alsaab, P.-Y. Chen, and J. L. Guo, "Optically transparent metasurface radome for RCS reduction and gain enhancement of multifunctional antennas," *IEEE Trans. Antennas Propag.*, vol. 71, no. 1, pp. 67–77, Jan. 2023.

[27] P. P. Shome, T. Khan, S. K. Koul, and Y. M. M. Antar, "Filtenna designs for radio-frequency front-end systems: A structural-oriented review," *IEEE Antennas Propag. Mag.*, vol. 63, no. 5, pp. 72–84, Oct. 2021.

[28] R. H. Mahmud and M. J. Lancaster, "High-gain and wide-bandwidth filtering planar antenna array-based solely on resonators," *IEEE Trans. Antennas Propag.*, vol. 65, no. 5, pp. 2367–2375, May 2017.

[29] Y.-M. Zhang, S. Zhang, G. Yang, and G. F. Pedersen, "A wideband filtering antenna array with harmonic suppression," *IEEE Trans. Microw. Theory Techn.*, vol. 68, no. 10, pp. 4327–4339, Oct. 2020.

[30] S. Wu, J. Li, X. Chen, S. Yan, and X. Y. Zhang, "A *Ka*-band SLM printed filtering divider-fed magnetoelectric dipole antenna array using embedded gap waveguide," *IEEE Antennas Wireless Propag. Lett.*, vol. 22, no. 4, pp. 774–778, Apr. 2023.

[31] H.-Y. Xie, B. Wu, L.-W. Song, Y.-L. Xin, J.-Z. Chen, and T. Su, "High-gain third-order filtering patch antenna array with two radiation nulls using cross-radiation," *IEEE Trans. Circuits Syst. II, Exp. Briefs*, vol. 70, no. 11, pp. 4053–4057, Nov. 2023, doi: 10.1109/TCSII.2023.3283262.

[32] T. Le-Huu, S. X. Ta, K. K. Nguyen, C. Dao-Ngoc, and N. Nguyen-Trong, "Differential-fed dual-polarized filtering Fabry–Pérot antenna with high isolation," *IEEE Access*, vol. 10, pp. 94616–94623, 2022.

[33] G. V. Trentini, "Partially reflecting sheet arrays," *IRE Trans. Antennas Propag.*, vol. 4, no. 4, pp. 666–671, Oct. 1956.

[34] A. P. Feresidis and J. C. Vardaxoglou, "High gain planar antenna using optimised partially reflective surfaces," *IEE Proc. Microw., Antennas Propag.*, vol. 148, no. 6, pp. 345–355, 2001.

[35] J.-D. Zhang, L. Zhu, Q.-S. Wu, N.-W. Liu, and W. Wu, "A compact microstrip-fed patch antenna with enhanced bandwidth and harmonic suppression," *IEEE Trans. Antennas Propag.*, vol. 64, no. 12, pp. 5030–5037, Dec. 2016.

[36] S. X. Ta and N. Nguyen-Trong, "Analysis and design of an ultrawideband dual-polarized antenna for IBFD applications," *IEEE Trans. Antennas Propag.*, vol. 70, no. 11, pp. 11121–11126, Nov. 2022.

TRUONG LE-HUU received the Engineering degree in electronics and telecommunications from the Hanoi University of Science and Technology (HUST), Vietnam, in July 2006, the Master of Engineering degree in electronic engineering from Dongguk University, South Korea, in February 2009. He is currently pursuing the Ph.D. degree with HUST. From March 2009 to November 2018, he was with the Viettel Group, where he was pointed to the Vice Director of Engineering of the Radar Institute, in 2012. From November 2018 to April 2021, he was a Technical Sales Engineer with Richardson RFPD Inc. Since April 2021, he has been the Director of the Electronic Platform Center, Viettel Aerospace Institute, Viettel Group. His research interests include antennas, RF transceiver, RF power amplifier systems, radar, and electronic warfare.

HAI DANG LE (Member, IEEE) is currently pursuing the B.Sc. (Eng.) degree in electrical and electronic engineering with the Hanoi University of Science and Technology (HUST), Vietnam. Since 2021, he has been as an Internship Researcher with the Communication Research and Development Laboratory (CRD-Lab), HUST. His research interests include microstrip patch antennas, metasurfaces, metasurface-based antennas, dual circularly-polarized antennas, differential-circuits, and Fabry-Perot antennas.

SON XUAT TA (Senior Member, IEEE) received the B.Sc. (Eng.) degree in electronics and telecommunications from the Hanoi University of Science and Technology (HUST), Vietnam, in August 2008, and the Ph.D. degree in electrical engineering from Ajou University, South Korea, in February 2016. From March 2016 to February 2017, he was a Postdoctoral Research Fellow with the Department of Electrical and Computer Engineering, Ajou University. From March 2017 to August 2017, he was with the Division of Computational Physics, Institute for Computational Science, and the Faculty of Electrical and Electronics Engineering, Ton Duc Thang University, Ho Chi Minh City, Vietnam. Since September 2017, he has been a Lecturer with the School of Electronics and Telecommunication (now renamed as the School of Electrical and Electronic Engineering), HUST. His research interests include antennas, metamaterials, metasurfaces, metamaterial-based antennas, metasurface-inspired antennas, circularly polarized antennas, and millimeter-wave antennas. He has authored and coauthored over 100 technical journals and conference papers. He has served as a reviewer for over 15 scientific journals. He has been selected as a Top Reviewer for IEEE TRANSACTIONS ON ANTENNAS AND PROPAGATION, in 2020, 2021, and 2022.

KHAC KIEM NGUYEN (Member, IEEE) was born in Hanoi, Vietnam, in 1978. He received the B.Eng., M.Sc., and Ph.D. degrees from the School of Electronics and Telecommunication—SET (now renamed as School of Electrical and Electronic Engineering—SEEE), Hanoi University of Science and Technology (HUST), Vietnam, in 2001, 2003, and 2017, respectively. Since 2001, he has been a Lecturer with SEEE, HUST, and a Researcher with the CRD Laboratory, HUST. His research interests include design microstrip antenna for next generation mobile communication systems and passive RF components.

NGHIA NGUYEN-TRONG (Senior Member, IEEE) received the Ph.D. degree (Hons.) in electrical engineering from The University of Adelaide, Adelaide, SA, Australia, in 2017.

He is currently a Lecturer with The University of Adelaide. His main research interests include microwave circuits, advanced materials, absorbers, and the various types of antennas.

Dr. Nguyen-Trong was one of a recipient of the Best Student Paper Award at the 2014 IWAT, the 2015 IEEE MTT-S NEMO, and the 2017 ASA Conferences, and the Best Paper Award at the 2018 and 2020 AMS Conference. He has been continuously selected as a Top Reviewer for IEEE TRANSACTIONS ON ANTENNAS AND PROPAGATION, in 2018, 2019, 2020, and 2021, and IEEE ANTENNA WIRELESS AND PROPAGATION LETTERS, in 2018 and 2021. He serves as the Technical Co-Chair for the 2020 Australian Microwave Symposium (AMS) and 2022 IEEE International Symposium on Antennas and Propagation. He is listed among Australia's Top 40 Early Career Researchers by the Australian, in November 2021.